The *App^NL-G-F* mouse retina is a site for preclinical Alzheimer's disease diagnosis and research

Marjan Vandenabeele[1,2], Lien Veys[1,2], Sophie Lemmens[3], Xavier Hadoux[4], Géraldine Gelders[1,2], Luca Masin[1,2], Lutgarde Serneels[2,5], Jan Theunis[6], Takashi Saito[7,8], Takaomi C. Saido[7], Murali Jayapala[9], Patrick De Boever[6,10], Bart De Strooper[2,5], Ingeborg Stalmans[3], Peter van Wijngaarden[4], Lieve Moons[1,2], Lies De Groef[1,2]*

[1]KU Leuven, Neural Circuit Development and Regeneration Research Group, Department of Biology, Leuven, Belgium

[2]Leuven Brain Institute, Leuven, Belgium

[3]University Hospitals Leuven, Department of Ophthalmology, Leuven, Belgium; KU Leuven, Research Group Ophthalmology, Department of Neurosciences, Leuven, Belgium

[4]Centre for Eye Research Australia, Royal Victorian Eye and Ear Hospital, East Melbourne, Australia; Ophthalmology, Department of Surgery, University of Melbourne, Parkville, Australia

[5]VIB Center for Brain & Disease Research, Leuven, Belgium; KU Leuven, Laboratory for the Research of Neurodegenerative Diseases, Department of Neurosciences, Leuven, Belgium

[6]VITO (Flemish Institute for Technological Research), Health Unit, Mol, Belgium

[7]Laboratory for Proteolytic Neuroscience, RIKEN Center for Brain Science, Saitama, Japan

[8]Department of Neurocognitive Science, Institute of Brain Science, Nagoya City University Graduate School of Medical Sciences, Japan

[9]Imec (Interuniversity Microelectronics Centre), Leuven, Belgium

[10] Hasselt University, Center of Environmental Sciences, Diepenbeek, Belgium; University of Antwerp, Department of Biology, Wilrijk, Belgium

*Corresponding author:

Lies De Groef

Neural Circuit Development and Regeneration Research Group

Department of Biology

University of Leuven (KU Leuven)

Naamsestraat 61, box 2464

3000 Leuven

Belgium

Tel. + 32 (0)16 37 37 64

Abstract

In this study, we report the results of a comprehensive phenotyping of the retina of the *App^NL-G-F* mouse. We demonstrate that soluble Aβ accumulation is present in the retina of these mice early in life and progresses to Aβ plaque formation by midlife. This rising Aβ burden coincides with local microglia reactivity, astrogliosis, and abnormalities in retinal vein morphology. Electrophysiological recordings reveal signs of neuronal dysfunction yet no neurodegeneration was observed and visual performance outcomes were unaffected in the *App^NL-G-F* mouse. Furthermore, we show that hyperspectral imaging can be used to quantify retinal Aβ, underscoring its potential as a biomarker for AD diagnosis and monitoring. These findings suggest that the *App^NL-G-F* retina mimics the early, preclinical stages of AD, and, together with retinal imaging techniques, offers unique opportunities for drug discovery and fundamental research into preclinical AD.

I.   Introduction

Alzheimer's disease (AD) is the number one neurodegenerative disorder and cause of dementia. Accumulation of amyloid-beta (Aβ) plaques and hyperphosphorylated Tau in tangles are two hallmarks of AD, and are believed to lead to neurotoxic inflammation, neuronal dysfunction, and eventually neurodegeneration. Despite decades of research, the AD field is still struggling with finding techniques for adequate diagnosis and disease monitoring, rational treatment strategies and valid research models.

AD is supposed to start 20 years before the first cognitive symptoms appear[1–3], and it is nowadays believed that one should focus on this time window for diagnosis and future treatment[4,5]. In the search for new biomarkers and animal models that allow evaluation of this preclinical phase of AD, increasing attention has gone to the retina. Indeed, given that the retina is an integral part of the central nervous system, cellular and molecular mechanisms underlying neurodegeneration are conserved, and pathological processes occurring in the retina may be an indicator of those processes ongoing in other parts of the central nervous system[6,77,8]. In addition, state-of-the-art technologies for ocular imaging (e.g. optical coherence tomography and confocal scanning laser ophthalmoscopy) allow these processes to be visualised at a resolution of at least an order of a magnitude higher than conventional brain imaging techniques, without the need for invasive, costly procedures or tracers, and in a reproducible and quantifiable manner[7].

One emerging technique in the field of retinal biomarkers for AD, is retinal hyperspectral imaging. This non-invasive imaging spectroscopy technique relies on the wavelength-dependent effect of Aβ on light scatter, to measure the reflectance spectrum of a locus over a range of wavelengths and convert this into a hyperspectral score of which the magnitude correlates to the amount of Aβ. The exact pathological correlate of this hyperspectral signature is still unclear, although previous *in vitro* studies and theoretical modeling suggested that soluble Aβ$_{42}$ is being measured[9,10]. The latter would be a particular advantage, as converging evidence suggests that, in the preclinical phase of AD, soluble oligomeric Aβ accumulates to a threshold that eventually leads to symptomatic AD. Rather than intermediates to generation of Aβ plaques, these Aβ oligomers are nowadays regarded as being the most pathogenic form of Aβ. Aβ oligomers initiate neuropathological processes such as neuroinflammation, gliosis, degradation of synapses, impaired axonal transport, and oxidative damage, thereby leading to an enlarging pool of neurons with limited functionality and ultimately driving the diseased brain to the tipping point where actual neurodegeneration ensues[11–14].

A multitude of studies has evaluated the retinal phenotype of AD mouse models, and revealed retinal abnormalities that mirror observations in human AD subjects, including elevated Aβ levels, Aβ deposits co-localizing with sites of apoptosis, tauopathy, neurodegeneration of ganglion and amacrine cells, microgliosis and astrogliosis, abnormal electrophysiology, as well as tight junction attenuation and vessel malformations[15–19]. However, results are often conflicting and interpretation of their biological relevance is obscured by the fact that these transgenic AD mice all rely on ectopic overexpression of familial AD-associated genes (mutations). Here, we address this shortcoming with a comprehensive retinal phenotyping study of the App^{NL-G-F} knock-in mouse, which is characterized by physiological expression of humanized mouse APP, containing the Swedish, Beyreuther/Iberian and Arctic mutations, in disease-relevant central nervous system regions and cell types[20,21]. For this first-time retinal phenotyping study of the App^{NL-G-F} mouse, we heavily relied on *in vivo* techniques to assess the possibility of longitudinal disease monitoring via retinal imaging and electrophysiology, besides the gold standard *post mortem* assays. Additionally, we evaluated the use of hyperspectral imaging to quantify retinal Aβ burden, based on the hypothesis that it detects soluble $Aβ_{42}$ and therefore may offer a way to study preclinical AD. Altogether, this approach represents a novel tool box, with the retina of the App^{NL-G-F} mouse as a model and retinal imaging techniques as unique read-outs, for both fundamental and drug discovery research in the preclinical phase of AD.

II. Results

<u>Amyloid accumulates in the retinas of App^{NL-G-F} mice, with Aβ plaque formation at old age</u>

Retinal amyloid burden was studied in App^{NL-G-F} mice of various ages via ELISA. Soluble $Aβ_{42}$ was detected at 3 months, with stable levels until 18 months, yet a steep increase at 24 months (p=0.0006) (Fig. 1a). Insoluble $Aβ_{42}$, which is typically aggregated in amyloid plaques, was only clearly elevated at 12 months and dramatically increased at 24 months (p<0.0001) (Fig. 1a). In contrast, and in line with the combined effect of the Swedish mutation that increases total Aβ production and the Iberian mutation that increases the $Aβ_{42}/Aβ_{40}$ ratio, a steady level of soluble $Aβ_{40}$ accumulation was present from 3 to 24 months, albeit two orders of magnitude lower than $Aβ_{42}$ (Fig. 1b). Insoluble $Aβ_{40}$ (Fig. 1b) as well as soluble/insoluble $Aβ_{38}$ and $Aβ_{36}$ levels (data not shown) were below the detection limit of the assay. For comparison, in the APP/PS1 overexpression mouse model, at 18 months of age (when retinal plaques are present [22–26]), we detected the accumulation of soluble $Aβ_{42}$ (comparable levels to App^{NL-G-F}), soluble $Aβ_{40}$ (higher levels than App^{NL-G-F}), and insoluble $Aβ_{42}$ (lower levels than App^{NL-G-F}) (Fig. 1c).

4

In accordance with these results, Aβ plaques were detected via 6E10 and 82E1 immunohistochemistry on retinal wholemounts of App^{NL-G-F} mice of 18 months of age (Fig. 1d-k). Morphologically, these resembled classical brain plaques, with a dense core and radiating fibrillary arms. Sizes typically ranged from 5 to 20 µm. Aβ plaque density was higher in the peripheral than in the central retina, while no overt differences between the retinal quadrants were seen. Plaques were mainly localized in the inner plexiform layer (Fig. 1i), although some were found in the nerve fiber layer, often in close association with blood vessels (Fig. 1f, j).

These data show that, while soluble $Aβ_{42}$ (and $Aβ_{40}$) is present in the retinas of App^{NL-G-F} mice early in life, retinal Aβ plaques only appear from 18 months of age onwards. Given this relatively slow progression of amyloidopathy, this retinal mouse model may be used to study the conversion from early to late stages of AD pathogenesis, as well as the effect of soluble Aβ on retinal structure and function. For the characterization of the latter, in addition to longitudinal studies, we will largely focus on ages 3 and 18 months in the rest of this study, as these represent disease stages without and with Aβ plaques in the retina, respectively.

Hyperspectral imaging detects early retinal accumulation of Aβ in App^{NL-G-F} mice

Aiming to provide a proof-of-concept for the use of hyperspectral imaging for the early detection of retinal Aβ accumulation and for monitoring its progression, we next performed *ex vivo* hyperspectral imaging of retinal wholemounts of 3- and 18-month-old App^{NL-G-F} mice and age-matched WT controls. For both ages, the average spectra of the App^{NL-G-F} mice were clearly distinct from WT. In young mice, this separation was most marked in the 475-500 nm range (Fig. 2a), while in old mice the spectral separation became even more apparent, extending to 600 nm (Fig. 2b). A hyperspectral score was calculated for each mouse from the *ex vivo* retinal reflectance data, using a modification of methods developed for *in vivo* hyperspectral retinal imaging[27]. Hyperspectral scores were significantly higher in App^{NL-G-F} mice compared to age-matched WT mice at both ages (p=0.0014 at 3 months, p=0.0002 at 18 months) (Fig. 2d-e). Furthermore, the difference in the mean hyperspectral score of App^{NL-G-F} *versus* age-matched WT mice was also higher at 18 months than at 3 months, in line with the progressive accumulation of Aβ seen in the ELISA. Hyperspectral scores were calculated for each retinal quadrant in both central and peripheral locations (Fig. 2j). In keeping with the immunohistochemistry findings, which demonstrated a predominately peripheral distribution of Aβ, hyperspectral scores were higher in the peripheral retina than in the central retina (Fig. 2g-h).

Remarkably, 18-month-old APP/PS1 mice had retinal hyperspectral signatures that closely mimics those of 18-month-old App^{NL-G-F} mice (Fig. 2c, f, i). Given that these mice have similar levels of soluble $A\beta_{42}$, but markedly different levels of soluble $A\beta_{40}$ and insoluble $A\beta_{42}$, it is possible that soluble $A\beta_{42}$ is most contributory to the hyperspectral signature, as previously suggested by Vince and More[10].

<u>Neuronal dysfunction yet no degeneration in the inner retina of App^{NL-G-F} mice</u>

Many studies have shown neurotoxic effects of soluble Aβ, and that functional deficits may precede neurodegeneration. Therefore, first electroretinography was performed with App^{NL-G-F} and WT mice at different time points. Overall, no abnormalities were observed at early ages (Supplementary fig. 1). At 18 months, however, the latency of both the oscillatory potentials and the b-wave, a measure for amacrine and bipolar cell function, respectively, showed significant changes ($p<0.0001$ for the effect of genotype) in the App^{NL-G-F} mice relative to age-matched WT mice (Fig. 3d-g). Furthermore, also at 18 months of age, the latency of the a-wave was affected at the lowest light intensity ($p<0.0001$), suggesting compromised photoreceptor function (Fig. 3b-c).

Next, we assessed potential neurodegeneration in the App^{NL-G-F} retina via a longitudinal *in vivo* optical coherence tomography experiment. No differences in the overall thickness of the retina nor the nerve fiber, ganglion cell, inner plexiform or inner nuclear layers were identified at any age (Fig. 3h). Of note, no neurodegeneration was observed in the brains of the App^{NL-G-F} mice either[21]. A small decrease in the thickness of the outer nuclear layer was found in App^{NL-G-F} mice, from 12 months ($p=0.0016$ for 12 months, $p<0.0001$ for 18 months) of age onwards (Fig. 3i). Although these findings corroborate the electroretinogram results, we are unsure how to interpret their biological relevance given that this thinning is limited and occurs in the outer retina – where no plaques were seen.

Finally, based on the localization of plaques in the nerve fiber and inner plexiform layers, and in order to confirm and complement the optical coherence tomography data, we next examined neuronal subpopulations in the inner retinas of 18-month-old animals. We quantified: (i) ganglion cells, using the pan-ganglion cell marker RBPMS (Fig. 3l); (ii) melanopsin+ ganglion cells, given that this subtype appears to be selectively vulnerable to Aβ pathology[28] (Fig. 3m); and (iii) ChAT+ cholingeric amacrine cells (Fig. 3n). None of these neuronal subpopulations showed any sign of degeneration in the 18-month-old App^{NL-G-F} mice. In line with all of the above observations, and in keeping with neuroplasticity compensating for

6

neuron loss, 18-month-old App^{NL-G-F} mice behaved normally in the optomotor response test for visual acuity (Fig. 3o) and contrast sensitivity (data not shown).

Altogether, these results indicate that inner retinal neurons in the App^{NL-G-F} mouse survive progressive amyloidosis up till 18 months. Nevertheless, although no cell death was observed at this age, amacrine and bipolar cell function may be used as a sensitive read-out for AD pathology in the retina of App^{NL-G-F} mice.

Local microglia reactivity, astrogliosis and vascular changes in the retina of aged App^{NL-G-F} mice

Because of the strong implication of microgliosis and astrogliosis in AD pathogenesis, and as neurotoxic inflammation may precede neurodegeneration, we next examined the retinal glial cells. First, microgliosis was investigated in entire Iba1-labeled retinal wholemounts of App^{NL-G-F} mice aged between 3 and 18 months. Overall quantification of microglial density (Fig. 4a), soma size (Fig. 4b) and roundness (data not shown) did not reveal population-wide differences between the two genotypes at any age. Analysis of 18-month-old App^{NL-G-F} x $CX_3CR-1^{GFP/+}$ mice retinas, with GFP-labeled microglia, confirmed these findings (data not shown). However, a detailed investigation of these retinas, co-labeled for 6E10, revealed local microglia reactivity around Aβ plaques, as was previously shown in the brains of these mice[21] and in the retinas of other AD mouse models (3xTgAD, APP/PS1)[19,29,30]. Indeed, microglia clustered around Aβ plaques, and these cells showed less ramified, thicker processes and larger somas (p=0.0112) compared to microglia in regions without plaques (Fig. 4c-g) or in wild type $CX_3CR-1^{GFP/+}$ mice. Second, Müller glia and astrocyte reactivity were assessed on transverse sections of the retina. Longitudinal assessment of Müller glia reactivity, by counting the number of GFAP-positive radial fibers, revealed higher reactivity in 18-month-old App^{NL-G-F} versus WT mice (p=0.0432) (Fig. 4h-j). Further substantiating these findings, and in line with the brain phenotype[21], analysis of the S100B immunopositive area, which is specific for astrocytes, showed astrogliosis in the retina of 18-month-old App^{NL-G-F} mice (p=0.0057) (Fig. 4 k-m).

Looking at non-neuronal cell types, besides glial cells, also vasculature may undergo pathological alterations in the context of AD. Changes in retinal blood vessel function and morphology, including branching complexity, vessel density and vessel diameter, are being explored as potential early biomarkers for AD[31–34]. Given that a subset of plaques was found closely associated with the retinal vasculature, we next assessed vessel morphology on retinal wholemounts stained with isolectin B4 (Fig. 5). Vessel density (Fig. 5a) and branching complexity (Fig. 5b) were unaltered in App^{NL-G-F} versus WT mice at 18 months of age. However, diameters of the retinal venules (Fig. 5c), yet not of the retinal arterioles

(Fig. 5d), were smaller in App^{NL-G-F} mice (p=0.0235). Of note, Shi *et al.* recently reported pericyte loss accompanying retinal vascular amyloidosis, hence the observed reduction in diameter may be a manifestation of this[35].

III.   Discussion

In this study, we investigated the extent to which AD-associated disease processes are present in the retina of the App^{NL-G-F} knock-in mouse, and whether they can be monitored via *in vivo* retinal imaging and electrophysiology. First, we demonstrated that soluble Aβ (mostly Aβ$_{42}$) accumulation is present early in life in these mice yet retinal Aβ plaques are only observable at 12 months of age and older. This rising Aβ burden in the retina coincides with local microglia reactivity, astrogliosis, and abnormalities in retinal vein morphology, and leads to compromised electrophysiological function of selected retinal neurons. No overt neurodegeneration was seen, however, and visual performance outcomes were intact. Altogether, these findings suggest that the App^{NL-G-F} retina resemble changes that occur in the brain in preclinical AD, during which Aβ accumulation instigates the earliest detrimental effects on astrocytes, microglia and vasculature, poses a stress on neuronal functionality but does not lead to overt functional impairment and neuronal death yet. Second, the data presented in this study suggest that there is an identifiable pre-plaque stage in AD in which only soluble forms of Aβ are present, followed by a phase in which soluble, oligomeric forms of Aβ are likely in equilibrium with plaques. The App^{NL-G-F} retina and reported retinal imaging techniques offer unique opportunities for further fundamental and preclinical research into this sequence of biological events over the course of preclinical AD. Hence, the App^{NL-G-F} mouse is not only the first AD model to accumulate Aβ without phenotypes related to APP overexpression and to more closely model human pathophysiology, its retina also is the first model organ to study preclinical AD. Combined with the available non-invasive, high-resolution imaging techniques and functional assessments of the retina, this creates a toolbox for researchers to shed new light on Aβ proteostasis and novel disease-modifying therapies focused thereon.

The rather mild phenotype is in stark contrast to observations made in the brains of App^{NL-G-F} mice. Indeed, previous studies have shown that (sub)cortical Aβ plaques appear at 2-4 months of age, with astrogliosis and microglial reactivity at 6-9 months, and cognitive impairment as early as 6 months[21]. The later formation of Aβ plaques in the App^{NL-G-F} retina could be due to lower expression levels of Aβ compared to the brain, as shown for other AD mouse models[36], or to different clearance rates. However, importantly, it confers a unique strength to the App^{NL-G-F} retina as a model for AD research, as it creates a time window

8

to investigate the earliest phases of AD pathogenesis and is closer to the slow disease progression seen in humans. A second asset of the *App*[NL-G-F] retina is that, by diverging from many other available AD models, its phenotype shows striking similarities to the neuropathological changes seen in retinas of human AD patients. This includes the size of the retinal plaques, which we found to be 5-10 times smaller than their counterparts in the brain[23,37]; the localization of these plaques to the inner retinal layers – where endogenous APP expression has been observed[38,39] – and associated with retinal blood vessels; as well as the microglial reactivity, astrocytosis and changes in retinal vessel morphology. Of note, the manifestations of retinal vascular amyloidosis are of particular interest in light of the recent findings by Shi *et al.,* who reported pericyte loss accompanying retinal vascular amyloidosis in the human AD retina [35]. With one exception[40], this phenotype is thus far unstudied in AD mouse models and our data suggest that the *App*[NL-G-F] retina can be used to further explore this retinal manifestation of AD. Notably, an explanation for the diverging and more severe phenotype of many other transgenic AD mouse models may be sought in the fact that those models are far removed from the human disease state, with non-endogenous promotors, overexpression of APP byproducts, PS1 mutation and/or abnormal APP and Aβ expression levels. This study is pioneering in that it is the first-time retinal phenotyping study of the *App*[NL-G-F] knock-in mouse, which was created to overcome all of the aforementioned artefacts and currently still is unique in its kind. Finally, we have also showcased here the unique potential of the retina for *in vivo* monitoring of structural and functional changes in AD. Of the battery of tests used, hyperspectral imaging and electroretinograms proved to be sensitive read-outs to asses AD disease status. Results from our *post mortem* studies suggest that these may in future studies be complemented with confocal scanning ophthalmoscopy for microgliosis and optical coherence tomography angiography or fundus imaging for detailed retinal vascular assessments. Together, this creates a set of *in vivo* read-outs for preclinical investigation that cannot be matched by any existing *in vivo* brain research methods. Notably, the fact that identical techniques and outcome measures can be used in mice and patients, confers potential translational value to this research.

A better understanding of the time course of the pathological processes underlying preclinical AD, is an important prerequisite for the development of new therapies targeting this phase. Furthermore, retinal imaging may provide an accurate and convenient indication of the efficacy of therapies. Currently, Aβ status is evaluated via CSF assays or PET imaging, which is mainly indicative for the deposition of fibrillary forms of Aβ. As such, these do not always provide information about oligomeric Aβ, which may be the more relevant Aβ species to target[41,42]. Our data substantiate that hyperspectral imaging is a highly

9

sensitive technique that can be used to quantify Aβ burden in the earliest stages of disease. This imaging spectroscopy technique is based on the fact that soluble Aβ aggregates – most likely $A\beta_{42}$ – interfere with traversing light, leading to Rayleigh light scattering and a characteristic hyperspectral signature, the magnitude of which appear to be proportional to the amount of Aβ present[9,10]. In the past year, following promising *post mortem* and *in vivo* studies in both animal and human retinas[9,10,43], results of the first clinical trial showing that *in vivo* retinal hyperspectral imaging can discriminate between Aβ PET-positive cases and controls emerged[27]. This, together with our data, suggests that hyperspectral imaging can be used to monitor retinal Aβ accumulation, with the potential to provide quantitative measures of Aβ oligomers. As such, hyperspectral imaging in the *App*[NL-G-F] retina may become a gateway to improved preclinical studies of the new generation of Aβ therapeutics. Finally, on the long run, this research may also lay the foundations for the rational use of this retinal imaging biomarker for AD diagnosis, disease monitoring, patient stratification and even population-wide screenings.

To conclude, decades of AD research have taught us that we should not try to unravel AD pathogenesis from a simple, neuron-centric perspective, or by assuming a linear series of events leading from Aβ accumulation to dementia. AD is to be understood as a complex pathological cascade, taking decades to gradually evolve from a clinically silent phase to dementia, that is driven by the proteopathic stress imposed by Aβ and Tau conformations, and feedback and feedforward responses of astrocytes, microglia, and vascular cells[44]. Research based on this new framework requires novel approaches, including mouse models that more closely mimic human pathophysiology and allow the study of the earliest, preclinical phases of AD. In this research, we have shown that the retina of *App*[NL-G-F] mice is a promising model for preclinical AD, in which Aβ oligomers accumulate and pathological cellular responses are elicited. Furthermore, we have added further evidence in support of the potential of hyperspectral imaging to quantify retinal Aβ burden and to serve as an AD biomarker. Altogether, the *App*[NL-G-F] retina and retinal imaging techniques are unique tools for both fundamental and drug discovery research in the preclinical phase of AD.

IV.   Materials and methods

<u>Animals</u>

B6.129S5-*App*tm3.1Tcs (here referred to as *App*[NL-G-F])[20,21], *App*[NL-G-F] x *CX₃CR-1*[GFP/+] (generated via crossing of *App*[NL-G-F] and B6.129P2-*Cx3cr1*tm1Litt (The Jackson Laboratory)), B6;C3Tg

(APPswe,PSEN1dE9)85Dbo/Mmjax (here referred to as APP/PS1) mouse lines and corresponding wild type (WT) controls, were bred under standard laboratory conditions. App^{NL-G-F} and WT female mice were sacrificed at 3, 6, 9, 12 and 18 months of age (± 1 month). Male mice were also included for the 18-month age group. All animal experiments were performed according to the European directive 2010/63/EU and approved by the KU Leuven institutional ethics committee for animal research.

Aβ extraction and ELISA detection

For soluble Aβ extraction, two retinas from one mouse were pooled and homogenized in lysis buffer (50 mM NaCl, 0.4 % diethanolamine, and protease inhibitor cocktail (Roche)). Samples were spun down and supernatant was centrifuged for 50 min at 100.000 x g. Supernatant containing the soluble Aβ fraction was collected. From the pellet, insoluble Aβ was extracted with GuHCl (6 M GuHCl/50 mM Tris-HCl) by sonication, incubation at 25°C for 60 min and centrifugation for 20 min at 170.000 x g. Aβ levels were determined via ELISA Meso Scale Discovery 96-well plates coated with antibodies for $A\beta_{40}$ JRFcAβ40/28 and $A\beta_{42}$ JRFcAβ42/26. JRFAβN/25 (human specific N-terminal epitope) labeled with sulfo-TAG was used as the detection antibody. Antibodies were provided by Dr. Marc Mercken (Janssen Pharmaceutica).

(Immuno)histochemistry

Following perfusion with 4% paraformaldehyde (PFA), eyes were enucleated and post-fixated in 4% PFA for 1 hour. For cryosections (12 µm), eyes went through a sucrose gradient series for cryoprotection prior to embedding in O.C.T. compound (Tissue-Tek, Sakura). For wholemount preparations, retinas were flatmounted and post-fixated for one hour in 4% PFA. For Aβ immunostaining and hyperspectral imaging of retinal wholemounts, no additional fixation was done.

Retinal cryosections were stained for glial acidic fibrillary protein (GFAP), S100 calcium binding protein B (S100B) or RNA-binding protein with multiple splicing (RBPMS). For GFAP, antigen retrieval was performed via proteinase K treatment (5 min, 2 µg/ml, Qiagen); for S100B and RBPMS, no antigen retrieval was used. After blocking, sections were incubated overnight with anti-GFAP (1:2000, #Z0334, DAKO), anti-S100B (1:600, #ab52642, Abcam) or anti-RBPMS (1:250, #1830-RBPMS, PhosphoSolutions) primary antibodies. For GFAP and S100B, an Alexa-conjugated secondary antibody (Invitrogen) was used; for RBPMS, a biotin-conjugated antibody (Jackson ImmunoResearch) followed by tyramide signal amplification (Perkin Elmer) was used. 4',6-diamidino-2-phenylindole (DAPI) was used as a nuclear counterstain.

For wholemount (immuno)staining, wholemounts were frozen for 15 min at -80°C, and incubated overnight with primary antibodies for melanopsin (1:5000, #AB-N38, Advanced Targeting Systems),

ionized calcium-binding adapter molecule 1 (Iba1; 1:1000, #019-19741, Wako), choline acetyltransferase (ChAT; 1:500, #AB144P, Millipore), green fluorescent protein (GFP; 1:500, #ab13970, Abcam) and Aβ (6E10, 1:500, #803001, BioLegend and 82E1, 1:300, #10323, Immuno-Biological Laboratories), or with biotinylated isolectin B4 (1:50, #B-1205, Vector Laboratories), followed by incubation with corresponding Alexa-conjugated secondary antibodies or Alexa-conjugated streptavidin (Invitrogen). For Aβ staining, a three-minute step in 100% formic acid was performed before freezing, as well as an extra blocking with goat anti-mouse Fab fragments (1:50, Jackson ImmunoResearch) for 1 hour.

Microscopy and image analysis

Microscopy was performed either via confocal or multiphoton imaging (Olympus FV1000 or FV1000-M; for Aβ, Iba1, Cx3cr1-GFP, ChAT and isolectin B4) or conventional fluorescence microscopy (Leica DM6; for melanopsin, GFAP and S100B). For confocal or multiphoton imaging of retinal wholemounts, mosaic z-stack images (step size 2-4 μm) were taken. Image analyses were performed using Fiji software[45], unless stated otherwise.

(i)   *Microglia numbers and morphological parameters* were analyzed on maximum intensity projection images of retinal wholemounts, as described previously[46].

(ii)   *Macroglia reactivity* was quantified on retinal sections by manually counting GFAP-immunopositive fibers at the inner plexiform-inner nuclear layer border[47]. GFAP+ fibers were counted over a length of 300 μm, on 20 images per mouse (two peripheral and two central images per section; five sections per mouse, including the central section containing the optic nerve head, and the sections located 240 and 480 μm anterior/posterior). For S100B, the immunopositive area was measured in the nerve fiber/ganglion cell layer over a length of 300 μm, on 20 images per mouse (*cfr*. above)[48].

(iii)   *Retinal vasculature* was analyzed on retinal wholemounts, on maximum intensity projections from the upper vasculature. Vessel density and branching complexity was analyzed with AngioTool software[49] on a binarized image. Retinal vessel diameter was measured manually at a distance of 300-400 μm from the optic nerve head; 5 measurements were averaged per vessel.

(iv)   *RBPMS+ retinal ganglion cells* were counted manually on retinal sections, over a distance of 300 μm, on 20 frames per mouse (*cfr.* above)[47].

(v)   *Melanopsin+ retinal ganglion cell* numbers were counted manually on wholemount images[50].

(vi) *ChAT⁺ cells* were counted in 3D, using the 'spots' module of Imaris software (version 7.4.2) on z-stack pictures of the wholemounts.

Optical coherence tomography

Upon general anesthesia and pupil dilatation (0.5% tropicamide, Tropicol, Théa), optical coherence tomography scans of the retina (1000 A-scans, 100 B-scans, 1.4 x 1.4 mm, Bioptigen Envisu R2200) were acquired. Retinal layer thickness was measured using InVivoVue Diver 3.0.8 software (Bioptigen), at 16 locations equally spaced around the optic nerve head and averaged per mouse.

Optomotor response test

Visual performance was tested using the virtual reality optomotor test (Optomotory, Cerebral Mechanics), as previously described[47]. Briefly, the mouse was place on a platform in the testing arena and, using the staircase method, the maximal spatial frequency of moving black-white stripes for which the optomotor reflex was still present, was determined.

Electroretinogram

Following overnight dark adaptation, electroretinograms (Celeris, Diagnosys) were recorded for anesthetized mice. Lens electrodes with integrated stimulators were placed on the cornea after pupil dilation (0.5% tropicamide, Tropicol, Théa and 15% phenylephrine, Théa). Eyes were alternately stimulated, and the electrode on the contralateral eye was used as a reference. Full-field flash electroretinogram was recorded at increasing flash intensities of 0.003, 0.01, 0.1, 1, 2.5 and 7.5 cd*s/m^2. For each intensity, 3 flashes were averaged. Inter-flash time increased from 5 s for the first two flash intensities, 10 s for the next two intensities to 30 and 45 s for the two last intensities. The scotopic threshold response was measured at $5*10^{-6}$ cd*s/m^2 and 50 flashes were averaged. Analysis was performed with Espion v6.59.9 software (Diagnosys), as previously described[47]. The scotopic threshold response amplitude was defined as the peak of the curve. Using a band pass filter (75-300 Hz), the oscillatory potentials on the rising part of the b-wave were retrieved and the area under the curve was calculated. The latency of the oscillatory potentials was defined for OP2[47].

Hyperspectral imaging

A hyperspectral visible and near-infrared snapscan camera (150 bands, 470-900 nm, Imec; HSI Snapscan software (version 1.2.0)) was mounted on a Leica DM6 microscope with LED light source (400-700 nm).

13

The snapscan camera acquires the hyperspectral image (2048 x 1536 pixels) by the movement of the linescan hyperspectral imaging sensor with on-chip filter technology on a miniaturized translation platform inside the camera body. Filters for each spectral band cover five adjacent pixel rows. The camera was used in stop-motion mode in steps of three pixel rows to reduce cross-talk between adjacent spectral bands and with HDR enabled (three frames) to reduce signal-to-noise ratio. Acquisition was set to cover only the 70 visible light spectral bands (471-691 nm). For hyperspectral imaging, retinal wholemounts were stained with DAPI, prior to mounting on a glass slide using a drop of saline and a cover slip. The transmission spectra of central (1 mm from the optic nerve head) and peripheral (2 mm from the optic nerve head) regions of each retinal quadrant were acquired using a 40x objective with the ganglion cell layer nuclei used as the focal plane.

Spectral analysis was performed using a modification of published methods[27]. In brief, recorded hyperspectral images were spatially resampled to 20% of their original size to smooth out acquisition noise. Each spectrum was normalized by the average spectral value of the three longest wavelengths (685, 687 and 691 nm). Pixels with spectral values above 1.5 and below zero were considered as outliers and masked out from further analysis. Spectral data from all mice were stacked in a matrix and a corresponding class label (AD or wild type control [CO]) was given for each entry. The spectral model was derived, corresponding to the between class covariance vector, that is, the average spectral difference between AD and CO normalized by the number of spectra present in each group. The hyperspectral score for a given spectral pixel was obtained by performing a dot product between the spectral pixel and the spectral model (*i.e.,* the sum for each wavelength of the product between the spectral pixel and the spectral model). The average spectral score for a given mouse was calculated using all spectral pixels of all the HS images collected for that mouse.

Statistical analysis

The employed statistical analyses and number of mice are stipulated in the respective figure legend. Analyses were performed using Prism v.8.2.1 (GraphPad). Differences were considered statistically significant for two-sided p-values < 0.05 (#, *p < 0.05; ##, **p < 0.01; ###, ***p < 0.001; ####, ****p < 0.0001; * for comparisons with baseline, # for comparisons between genotype).

V.   Data availability

The data sets generated and analyzed during the current study are available from the corresponding author upon reasonable request.

14

VI.   Acknowledgements

We thank Véronique Brouwers and Evelien Herinckx for their assistance with mouse breeding and experimentation; Wouter Charle, Toon Van Craenendonck and Arnout Standaert for advice on hyperspectral imaging; RIKEN BioResource Center for creation and distribution of the AppNL-G-F mice. MV, LV, LuM and LDG are fellows of the Research Foundation Flanders (FWO). This research was supported by the Alzheimer's Research Foundation (SAO-FRA), the European Union Horizon 2020 Research and Innovation Program (2014-2020) (HERALD project, granted by the ATTRACT consortium). The Centre for Eye Research Australia receives Operational Infrastructure Support from the Victorian Government. XH and PvW acknowledge funding support from the H & L Hecht Trust and the Yulgilbar Alzheimer's Research Program.

VII.   Author contributions

MV designed the study, performed experiments, analyzed the data and wrote the manuscript; LV, SL, GG performed experiments; XH, LS, JT, LuM analyzed the data; TS and TCS created the App^{NL-G-F} mice; SL, JT, MJ and LDG implemented the hyperspectral imaging set-up; PDB, IS, BDS, PvW supervised the study and reviewed the manuscript; LM supervised and designed the study, analyzed the data and wrote the manuscript, LDG supervised and designed the study, performed experiments, analyzed the data and wrote the manuscript.

VIII.   Competing interests

The authors declare the following competing interests: XH and PvW have filed an International (PCT) Patent Application No PCT/AU2019/000003 relating to retinal hyperspectral imaging. They are co-founders of Enlighten Imaging PTY LTD, a start-up company focused on developing novel retinal imaging solutions for neurological and retinal diseases.

IX.   Materials & Correspondence

Correspondence and material requests should be addressed to Lies De Groef.
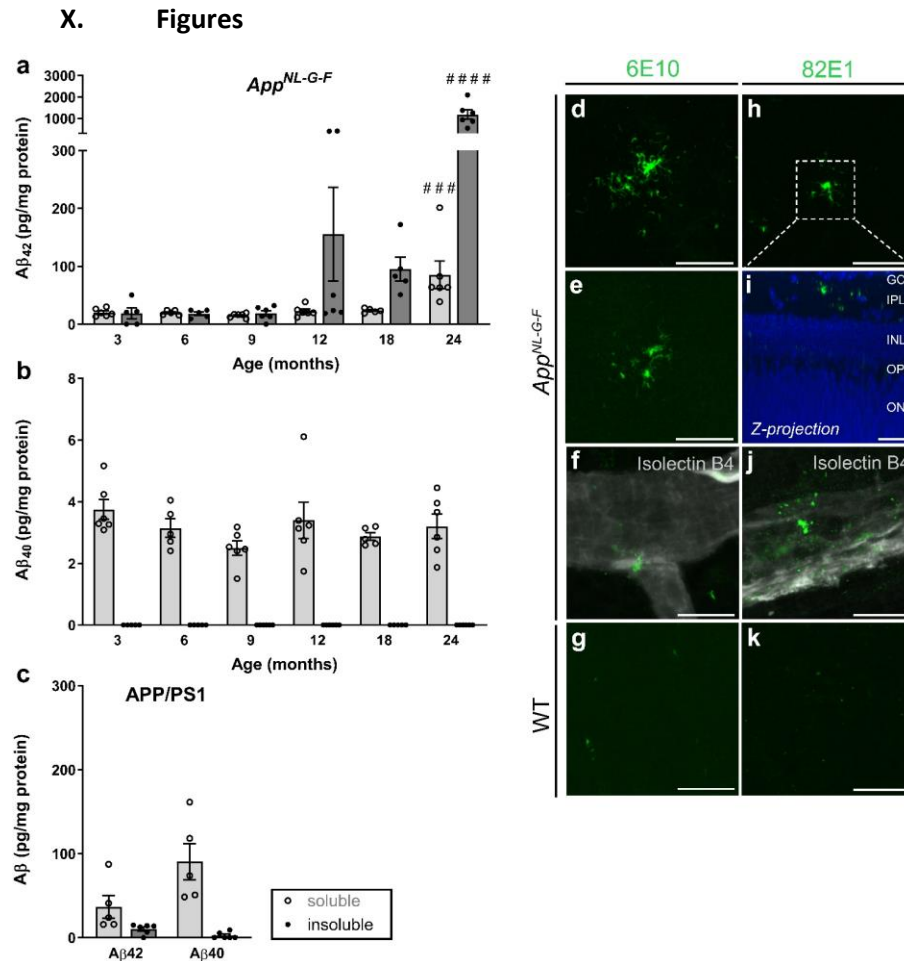
X.   Figures

Figure 1. Amyloid burden increases with age in the retina of App^{NL-G-F} mice. (a-b) Amyloid ELISA on retinal lysates of App^{NL-G-F} mice shows accumulation of soluble $A\beta_{42}$ from 3 months of age, which rises up till 24 months. Levels of insoluble $A\beta_{42}$ only start to rise at 12 months. Accumulation of soluble, but not insoluble, $A\beta_{40}$ is seen at all ages yet does not progress with age. One-way ANOVA with Dunnett's multiple comparisons test ($F_{5,28}=6.686$, $p=0.0006$ for soluble $A\beta_{42}$; $F_{5,27}=20.27$, $p<0.0001$ for insoluble $A\beta_{42}$); n=5-6. (c) Eighteen-month-old APP/PS1 mice have comparable soluble $A\beta_{42}$ levels yet lower levels of insoluble $A\beta_{42}$ and higher soluble $A\beta_{40}$ than App^{NL-G-F} mice of the same age. n=5. Of note, human $A\beta$ levels are undetectable in the retinas of WT mice and therefore these controls are not shown. (d-k) $A\beta$ immunostainings with antibodies 6E10 (d-g) and 82E1 (h-k) on retinal wholemounts of 18-month-old App^{NL-G-F} (d-f, h-j) and WT mice (g, k) reveal the presence of $A\beta$ plaques in App^{NL-G-F} mice only. (i) Example of a reconstruction of the z-plane of the image in panel h, with 82E1 and DAPI nuclear counterstaining, showing that plaques mainly localize to the inner plexiform layer. (f, j) Double labeling for amyloid and isolectin B4 shows that a subset of $A\beta$ plaques localizes around retinal blood vessels. Scalebar: 20 µm. Data are shown as mean $\pm$ SEM. GCL = ganglion cell layer, IPL = inner plexiform layer, INL = inner nuclear layer, OPL = outer plexiform layer, ONL = outer nuclear layer.

16
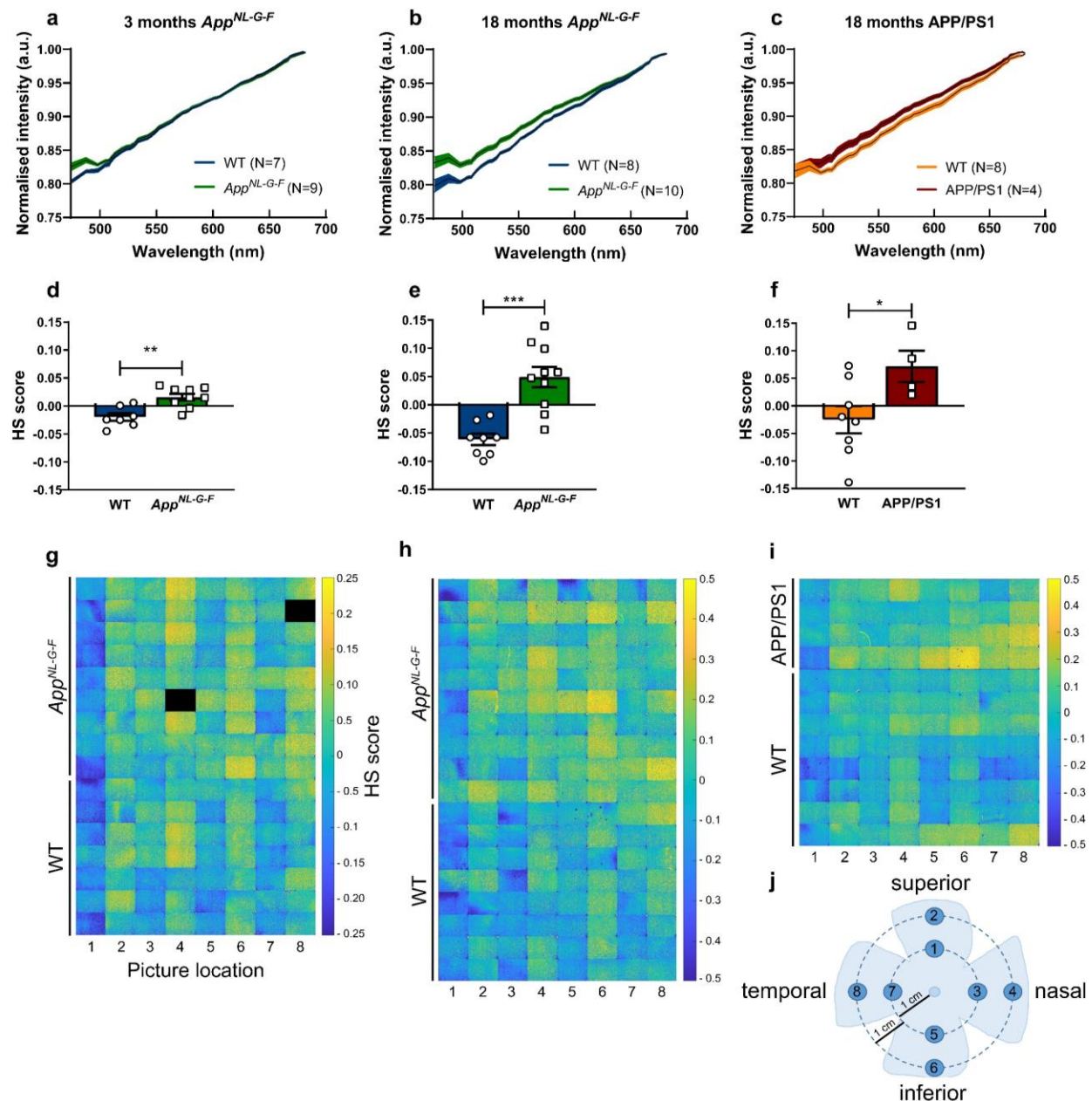
Figure 2. Quantification of retinal Aβ burden via hyperspectral imaging reveals progressive retinal amyloidosis in *App^{NL-G-F}* mice. (a) Average spectra of 3-month-old *App^{NL-G-F}* and WT mice are different, with a clear separation in the short wavelength range. (b) Average spectra of 18-month-old *App^{NL-G-F}* and WT mice show significant spectral differences for all wavelengths up to 600 nm. (c) Average spectra of 18-month-old APP/PS1 and WT mice show significant spectral differences from ~500 to ~600 nm. (d-e) For both ages, comparison of hyperspectral (HS) scores (obtained by compression of the spectral information to maximize between group separation) of *App^{NL-G-F}* and WT mice shows a strong effect size and significant difference between genotypes. Unpaired two-tailed t-tests (t_{14}=3.957,p=0.0014 at 3 months; t_{16}=4.919,p=0.0002 at 18 months); n=8-10. (f) HS scores of 18-month-old APP/PS1 and WT mice are significantly different. Unpaired two-tailed t-tests (t_{10}=2.395,p=0.0376); n=4-8. (g-i) Heatmaps with a spatial representation of the HS score per image for each mouse. Note that image fields 2, 4, 6 and 8,

which correspond to the peripheral retinal locations, have higher scores, indicative for a higher amyloid load. (j) Schematic representation of the retinal imaging locations.
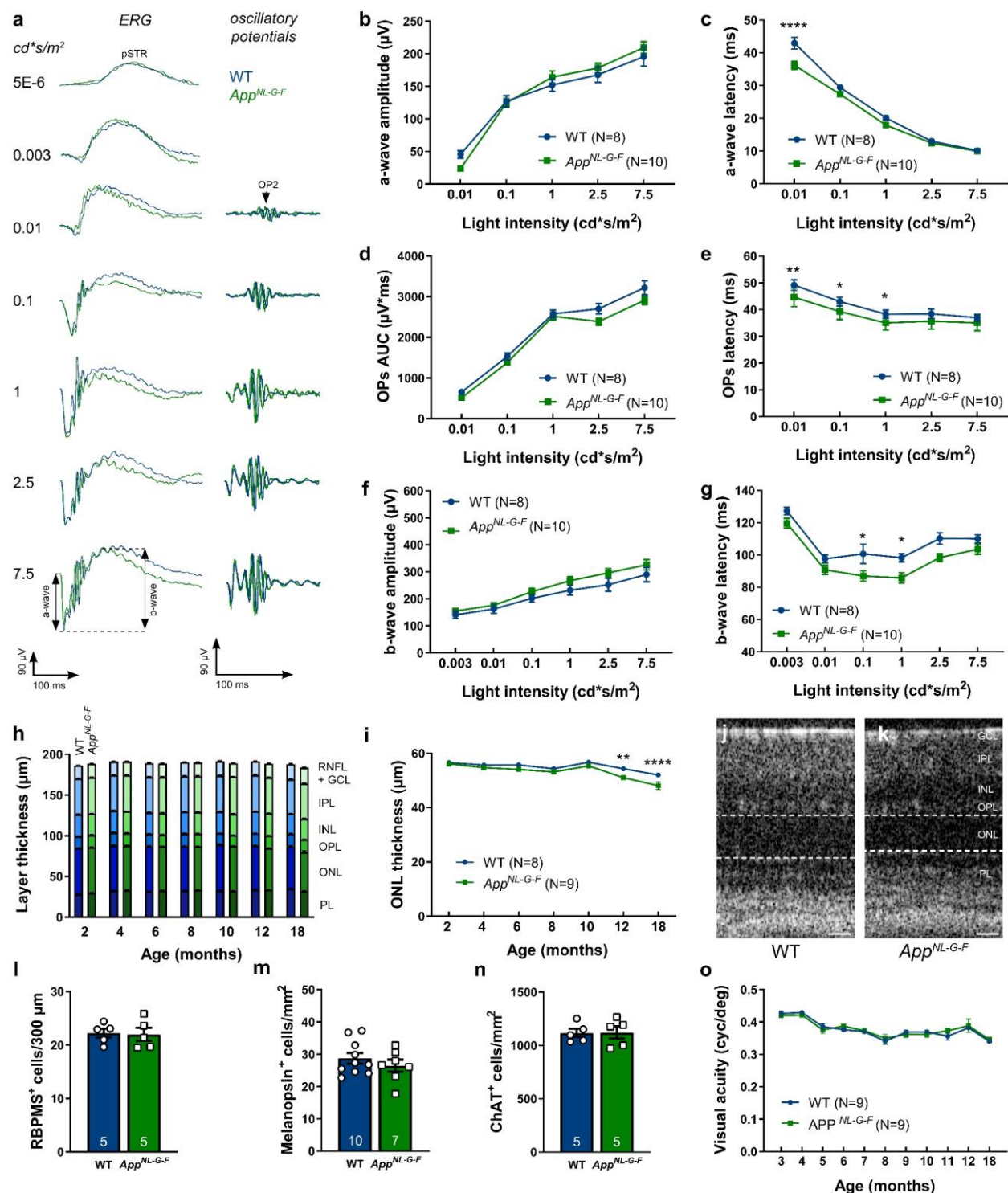
Figure 3. Neuronal dysfunction yet no degeneration in the inner retina of App^{NL-G-F} mice. (a) Representative electroretinogram measurements, with increasing light intensities, in 18-month-old App^{NL-G-F} (green) and WT (blue) mice. (b) The amplitude of the a-wave is unaffected in App^{NL-G-F} mice of 18 months, yet (c) the latency time is decreased for the lowest light intensity. Two-way ANOVA with Sidak's multiple comparisons test ($F_{1,85}$ = 23.14 for the effect of genotype, p<0.0001; n=8-10). (d) Oscillatory potentials show a similar wave front (measured as the area under the curve, AUC), but (e) a reduced
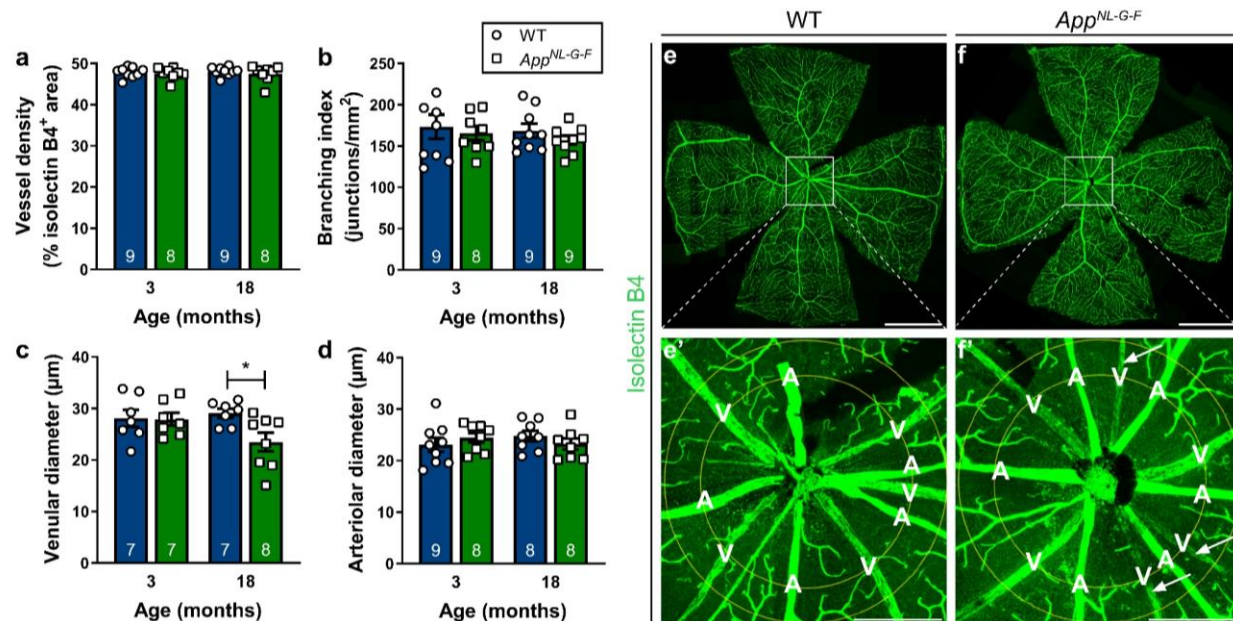
latency in 18-month-old App^{NL-G-F} mice, compared to WT. Two-way ANOVA with Sidak's multiple comparisons test ($F_{1,80}$ = 37.14 for the effect of genotype, p=0.0013, 0.0124, 0.0378 for 0.01, 0.1 and 1 cd*s/m^2 respectively); n=8-10. (f) Similarly, the amplitude of the b-wave is unaltered, but (g) the latency time is decreased in 18-month-old App^{NL-G-F} mice compared to WT mice. Two-way ANOVA with Sidak's multiple comparisons test ($F_{1,97}$ = 27.90 for the effect of genotype, p=0.0206 and 0.044 for 0.1 and 1 cd*s/m^2); n=8-10. Full electroretinogram data is given in Supplementary figure 1. (h) Analysis of the thickness of the retinal layers, as measured by optical coherence tomography, shows no differences between App^{NL-G-F} and WT mice from 2 to 18 months of age, (i) with the exception of a thinning of the outer nuclear layer. Two-way ANOVA with Sidak's multiple comparisons test ($F_{1,106}$ = 32.14 for the effect of genotype, p=0.0016 and p<0.0001 for 12 and 18 months, respectively); n=8-9. (j-k) Representative optical coherence tomography images of WT (j) and App^{NL-G-F} (k) retinas. Dotted lines delineate the outer nuclear layer. (l-n) Cell counts of RBPMS$^+$ retinal ganglion cells (l), melanopsin$^+$ ganglion cells (m) and ChAT$^+$ neurons (n) show no differences in numbers between 18-month-old App^{NL-G-F} and WT mice. (o) A longitudinal study of visual acuity in App^{NL-G-F} mice from 3 till 18 months revealed a decrease with age but no genotype differences. Two-way ANOVA ($F_{10,180}$=21.11 for the effect of age, $F_{1,180}$=0.1149 for the effect of genotype); n=9. Scale bar: 25 µm. Data are depicted as mean ± SEM; RNFL = retinal nerve fiber layer, GCL = ganglion cell layer, IPL = inner plexiform layer, INL = inner nuclear layer, OPL = outer plexiform layer, ONL = outer nuclear layer, PL = photoreceptor layer.
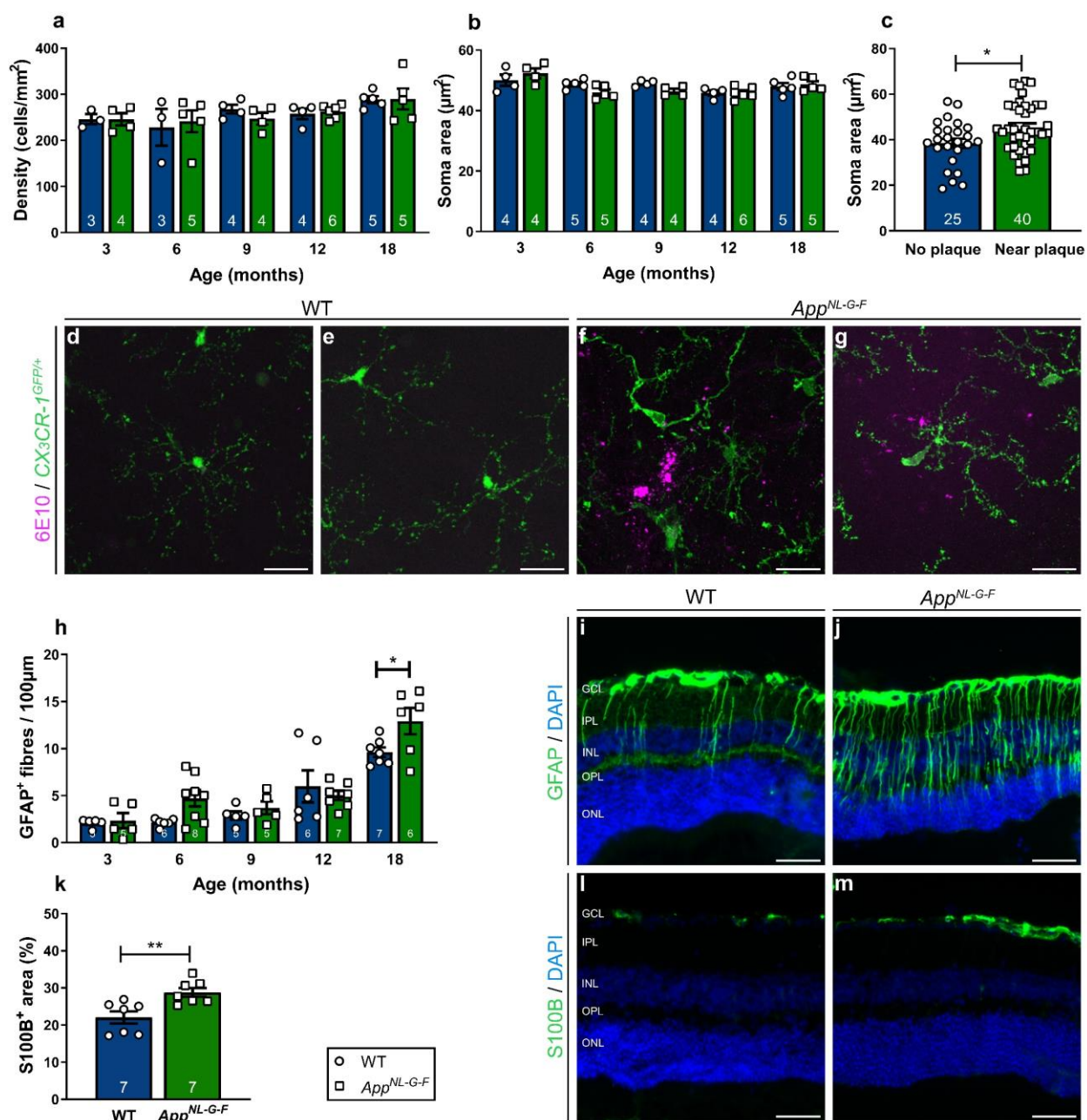
Figure 4. Locally reactivated microglia and macrogliosis in the retinas of aged *App^NL-G-F* mice. (a-b) Quantification of microglial density (a) and soma area (b) on Iba1-labeled retinal wholemounts of 3- to 18-month-old *App^NL-G-F* and WT mice reveals no differences between genotypes when analyzed for the entire retina. An effect of aging was observed for microglia density (Two-way ANOVA, $F_{4,33}$ = 2.976, p=0.0334); n=3-6. (c) Morphometric analysis of plaque-associated microglia *versus* microglia distant from Aβ plaques in 18-month-old *App^NL-G-F* x *CX₃CR-1^GFP/+* retinas reveals that plaque-associated microglia have a larger soma, which is indicative of their activation. Unpaired two-tailed t-test (t_{63}=2.614, p=0.0112); n=25-40 cells from 6 mice. (d-g) Representative images of immunostaining for Aβ (6E10) on retinal wholemounts of 18-month-old *App^NL-G-F* x *CX₃CR-1^GFP/+* (f-g) and *CX₃CR-1^GFP/+* mice (d-e), illustrating that green fluorescent microglia surrounding Aβ plaques display morphological alterations typical for reactive

21

microglia, with thicker and less ramified processes and a larger soma. (h) Counting the number of GFAP$^+$ radial fibers on retinal sections of App^{NL-G-F} and WT mice shows that macrogliosis increases with age, and significantly differs between genotypes at 18 months. Two-way ANOVA with Sidak's multiple comparisons test ($F_{4,50}$=34.02 for the effect of age, $F_{1,50}$=4.411 for the effect of genotype, p=0.0432); n=5-8. (i-j) Representative images of a GFAP immunostaining on retinal cross-sections of 18-month-old WT (i) and App^{NL-G-F} (j) mice. (k) Quantification of the S100B immunopositive area on retinal sections of 18-month-old App^{NL-G-F} and WT mice shows astrogliosis in the App^{NL-G-F} retina. Unpaired two-tailed t-test (t_{12}=3.358, p=0.0057); n=7. (l-m) Representative images of the S100B immunostaining on WT (l) and App^{NL-G-F} (m) retinas. Scalebar (d-g): 20 µm, scalebar (i, j, l, m): 50 µm. Data are shown as mean $\pm$ SEM. GCL = ganglion cell layer, IPL = inner plexiform layer, INL = inner nuclear layer, OPL = outer plexiform layer, ONL = outer nuclear layer.

Figure 5. Retinal venules of App^{NL-G-F} mice have reduced diameters. (a-b) Retinal vasculature was analyzed at 3 and 18 months of age. Quantification of the density of the vascular network (a) and its branching complexity (b) shows no differences according to genotype. (c-d) (c) Retinal venular diameters are reduced in 18-month-old App^{NL-G-F} mice. Two-way ANOVA with Sidak's multiple comparison's test ($F_{1,25}$=3.807 for the effect of genotype, p=0.0235); n=7-9 for 3 to 6 months, n=7-9 for 18 months. (d) No differences are seen in retinal arteriolar diameters. (e-f) Representative images of isolectin B4-labeled retinal flatmounts of 18-month-old WT (e) and App^{NL-G-F} (f) mice. (e'-f') Magnification of the region of interest in which vessel analysis was performed. Arrows indicate retinal venules with a reduced diameter. Scalebar: 1000 µm. Data are depicted as mean ± SEM. A = artery, V = vein.

XI.   References

1.   Jack, C. R. *et al.* Serial PIB and MRI in normal, mild cognitive impairment and Alzheimers disease: Implications for sequence of pathological events in Alzheimers disease. *Brain* (2009) doi:10.1093/brain/awp062.

2.   Reiman, E. M. *et al.* Brain imaging and fluid biomarker analysis in young adults at genetic risk for autosomal dominant Alzheimer's disease in the presenilin 1 E280A kindred: A case-control study. *Lancet Neurol.* **11**, 1048–1056 (2012).

3.   Villemagne, V. L. *et al.* Amyloid β deposition, neurodegeneration, and cognitive decline in sporadic Alzheimer's disease: A prospective cohort study. *Lancet Neurol.* **12**, 357–367 (2013).

4.   Sperling, R. A., Jack, C. R. & Aisen, P. S. Testing the right target and right drug at the right stage. *Science Translational Medicine* vol. 3 111cm33 (2011).

5.   Jack, C. R. *et al.* NIA-AA Research Framework: Toward a biological definition of Alzheimer's

disease. *Alzheimer's and Dementia* vol. 14 535–562 (2018).

6.   London, A., Benhar, I. & Schwartz, M. The retina as a window to the brain - From eye research to CNS disorders. *Nature Reviews Neurology* vol. 9 44–53 (2013).

7.   De Groef, L. & Cordeiro, M. F. Is the Eye an Extension of the Brain in Central Nervous System Disease? *J. Ocul. Pharmacol. Ther.* **34**, 129–133 (2018).

8.   Cordeiro, M. F. Eyeing the brain. *Acta Neuropathologica* vol. 132 765–766 (2016).

9.   More, S. S. & Vince, R. Hyperspectral imaging signatures detect amyloidopathy in alzheimers mouse retina well before onset of cognitive decline. *ACS Chem. Neurosci.* **6**, 306–315 (2015).

10.   More, S. S., Beach, J. M. & Vince, R. Early detection of amyloidopathy in Alzheimer's mice by hyperspectral endoscopy. *Investig. Ophthalmol. Vis. Sci.* **57**, 3231–3238 (2016).

11.   Cline, E. N., Bicca, M. A., Viola, K. L. & Klein, W. L. The Amyloid-β Oligomer Hypothesis: Beginning of the Third Decade. *Journal of Alzheimer's Disease* vol. 64 S567–S610 (2018).

12.   Fantini, J., Chahinian, H. & Yahi, N. Progress toward Alzheimer's disease treatment: Leveraging the Achilles' heel of Aβ oligomers ? *Protein science : a publication of the Protein Society* (2020) doi:10.1002/pro.3906.

13.   Wang, Z. X., Tan, L., Liu, J. & Yu, J. T. The Essential Role of Soluble Aβ Oligomers in Alzheimer's Disease. *Molecular Neurobiology* vol. 53 1905–1924 (2016).

14.   Harris, S. S., Wolf, F., De Strooper, B. & Busche, M. A. Tipping the Scales: Peptide-Dependent Dysregulation of Neural Circuit Dynamics in Alzheimer's Disease. *Neuron* (2020) doi:10.1016/j.neuron.2020.06.005.

15.   Hart, N. J., Koronyo, Y., Black, K. L. & Koronyo-Hamaoui, M. Ocular indicators of Alzheimer's: exploring disease in the retina. *Acta Neuropathologica* vol. 132 767–787 (2016).

16.   Lim, J. K. H. *et al.* The eye as a biomarker for Alzheimer's disease. *Frontiers in Neuroscience* vol. 10 536 (2016).

17.   Parnell, M., Guo, L., Abdi, M. & Cordeiro, M. F. Ocular manifestations of Alzheimer's disease in animal models. *International Journal of Alzheimer's Disease* (2012) doi:10.1155/2012/786494.

18.   Criscuolo, C. *et al.* The retina as a window to early dysfunctions of Alzheimer's disease following studies with a 5xFAD mouse model. *Neurobiol. Aging* **67**, 181–188 (2018).

19.   Grimaldi, A. *et al.* Inflammation, neurodegeneration and protein aggregation in the retina as ocular biomarkers for Alzheimer's disease in the 3xTg-AD mouse model. *Cell Death Dis.* **9**, 1–10 (2018).

20.   Nilsson, P., Saito, T. & Saido, T. C. New mouse model of Alzheimer's. *ACS Chemical Neuroscience* (2014) doi:10.1021/cn500105p.

21.   Saito, T. *et al.* Single App knock-in mouse models of Alzheimer's disease. *Nat. Neurosci.* (2014) doi:10.1038/nn.3697.

22.   Ning, A., Cui, J., To, E., Ashe, K. H. & Matsubara, J. Amyloid-β deposits lead to retinal degeneration in a mouse model of Alzheimer disease. *Investig. Ophthalmol. Vis. Sci.* (2008) doi:10.1167/iovs.08-1849.

23.   Koronyo-Hamaoui, M. *et al.* Identification of amyloid plaques in retinas from Alzheimer's patients and noninvasive in vivo optical imaging of retinal plaques in a mouse model. *Neuroimage* **54**, S204 (2011).

24.   Gupta, V. K. *et al.* Amyloid β accumulation and inner retinal degenerative changes in Alzheimer's disease transgenic mouse. *Neurosci. Lett.* (2016) doi:10.1016/j.neulet.2016.04.059.

25.   Yang, Y. *et al.* Suppressed Retinal Degeneration in Aged Wild Type and APPswe/PS1ΔE9 Mice by Bone Marrow Transplantation. *PLoS One* (2013) doi:10.1371/journal.pone.0064246.

26.   Georgevsky, D., Retsas, S., Raoufi, N., Shimoni, O. & Golzan, S. M. A longitudinal assessment of retinal function and structure in the APP/PS1 transgenic mouse model of Alzheimer's disease. *Transl. Neurodegener.* (2019) doi:10.1186/s40035-019-0170-z.

27.   Hadoux, X. *et al.* Non-invasive in vivo hyperspectral imaging of the retina for potential biomarker use in Alzheimer's disease. *Nat. Commun.* **10**, 1–12 (2019).

28.   La Morgia, C. *et al.* Melanopsin retinal ganglion cell loss in Alzheimer disease. *Ann. Neurol.* **79**, 90–109 (2016).

29.   Salobrar-García, E. *et al.* Microglial activation in the retina of a triple-transgenic alzheimer's disease mouse model (3xTg-AD). *Int. J. Mol. Sci.* (2020) doi:10.3390/ijms21030816.

30.   Perez, S. E., Lumayag, S., Kovacs, B., Mufson, E. J. & Xu, S. β-amyloid deposition and functional impairment in the retina of the APPswe/PS1ΔE9 transgenic mouse model of Alzheimer's disease. *Investig. Ophthalmol. Vis. Sci.* (2009) doi:10.1167/iovs.08-2384.

31.   Feke, G. T., Hyman, B. T., Stern, R. A. & Pasquale, L. R. Retinal blood flow in mild cognitive impairment and Alzheimer's disease. *Alzheimer's Dement. Diagnosis, Assess. Dis. Monit.* (2015) doi:10.1016/j.dadm.2015.01.004.

32.   Williams, M. A. *et al.* Retinal microvascular network attenuation in Alzheimer's disease. *Alzheimer's Dement. Diagnosis, Assess. Dis. Monit.* (2015) doi:10.1016/j.dadm.2015.04.001.

33.   Querques, G. *et al.* Functional and morphological changes of the retinal vessels in Alzheimer's disease and mild cognitive impairment. *Sci. Rep.* (2019) doi:10.1038/s41598-018-37271-6.

34.   Zabel, P. *et al.* Comparison of retinal microvasculature in patients with Alzheimer's disease and primary open-angle glaucoma by optical coherence tomography angiography. *Investig. Ophthalmol. Vis. Sci.* (2019) doi:10.1167/IOVS.19-27028.

35.   Shi, H. *et al.* Identification of early pericyte loss and vascular amyloidosis in Alzheimer's disease retina. *Acta Neuropathol.* **139**, 813–836 (2020).

36.   Alexandrov, P. N., Pogue, A., Bhattacharjee, S. & Lukiw, W. J. Retinal amyloid peptides and complement factor H in transgenic models of Alzheimer's disease. *Neuroreport* (2011) doi:10.1097/WNR.0b013e3283497334.

37.   Koronyo, Y. *et al.* Retinal amyloid pathology and proof-of-concept imaging trial in Alzheimer's disease. *JCI insight* **2**, (2017).

38.   Ho, T. *et al.* Amyloid precursor protein is required for normal function of the rod and cone pathways in the mouse retina. *PLoS One* (2012) doi:10.1371/journal.pone.0029892.

39.   Loffler, K. U., Edward, D. P. & Tso, M. O. M. Immunoreactivity against tau, amyloid precursor protein, and beta-amyloid in the human retina. *Investig. Ophthalmol. Vis. Sci.* (1995).

40.   Harper, D. J. *et al.* Retinal analysis of a mouse model of Alzheimer's disease with multicontrast optical coherence tomography. *Neurophotonics* **7**, 1 (2020).

41.   Sperling, R. A. *et al.* Toward defining the preclinical stages of Alzheimer's disease: Recommendations from the National Institute on Aging-Alzheimer's Association workgroups on diagnostic guidelines for Alzheimer's disease. *Alzheimer's Dement.* **7**, 280–292 (2011).

42.   Tolar, M., Abushakra, S. & Sabbagh, M. The path forward in Alzheimer's disease therapeutics: Reevaluating the amyloid cascade hypothesis. *Alzheimer's Dement.* (2020) doi:10.1016/j.jalz.2019.09.075.

43.   More, S. S., Beach, J. M., McClelland, C., Mokhtarzadeh, A. & Vince, R. In Vivo Assessment of Retinal Biomarkers by Hyperspectral Imaging: Early Detection of Alzheimer's Disease. *ACS Chem. Neurosci.* **10**, 4492–4501 (2019).

44.   De Strooper, B. & Karran, E. The Cellular Phase of Alzheimer's Disease. *Cell* vol. 164 603–615 (2016).

45.   Schindelin, J. *et al.* Fiji: An open-source platform for biological-image analysis. *Nature Methods* vol. 9 676–682 (2012).

46.   Davis, B. M., Salinas-Navarro, M., Cordeiro, M. F., Moons, L. & Groef, L. De. Characterizing microglia activation: A spatial statistics approach to maximize information extraction. *Sci. Rep.* **7**, 1–12 (2017).

47.   Sergeys, J. *et al.* Longitudinal in vivo characterization of the streptozotocin-induced diabetic mouse model: Focus on early inner retinal responses. *Investig. Ophthalmol. Vis. Sci.* (2019) doi:10.1167/iovs.18-25372.

48.   Van Hove, I. *et al.* Single-cell transcriptome analysis of akimba retina reveals cell type-specific insights into the pathobiology of diabetic retinopathy. *Diabetologia*.

49.   Zudaire, E., Gambardella, L., Kurcz, C. & Vermeren, S. A Computational Tool for Quantitative Analysis of Vascular Networks. *PLoS One* **6**, e27385 (2011).

50.   Valiente-Soriano, F. J. *et al.* Distribution of melanopsin positive neurons in pigmented and albino mice: evidence for melanopsin interneurons in the mouse retina. *Front. Neuroanat.* (2014) doi:10.3389/fnana.2014.00131.